HHS Public Access

Author manuscript

Magn Reson Med. Author manuscript; available in PMC 2017 June 01.

Published in final edited form as:

Magn Reson Med. 2016 June ; 75(6): 2481–2492. doi:10.1002/mrm.25776.

Multiscale Reconstruction for Magnetic Resonance Fingerprinting

Eric Y. Pierre[1], **Dan Ma**[1], **Yong Chen**[2], **Chaitra Badve**[2], and **Mark A. Griswold**[1,2]

[1]Department of Biomedical Engineering, Case Western Reserve University, Cleveland, Ohio, USA

[2]Department of Radiology, Case Western Reserve University & University Hospitals, Cleveland, Ohio, USA

Abstract

Purpose—To reduce acquisition time needed to obtain reliable parametric maps with Magnetic Resonance Fingerprinting.

Methods—An iterative-denoising algorithm is initialized by reconstructing the MRF image series at low image resolution. For subsequent iterations, the method enforces pixel-wise fidelity to the best-matching dictionary template then enforces fidelity to the acquired data at slightly higher spatial resolution. After convergence, parametric maps with desirable spatial resolution are obtained through template matching of the final image series. The proposed method was evaluated on phantom and in-vivo data using the highly-undersampled, variable-density spiral trajectory and compared with the original MRF method. The benefits of additional sparsity constraints were also evaluated. When available, gold standard parameter maps were used to quantify the performance of each method.

Results—The proposed approach allowed convergence to accurate parametric maps with as few as 300 time points of acquisition, as compared to 1000 in the original MRF work. Simultaneous quantification of T1, T2, proton density (PD) and B_0 field variations in the brain was achieved in vivo for a 256×256 matrix for a total acquisition time of 10.2s, representing a 3-fold reduction in acquisition time.

Conclusions—The proposed iterative multiscale reconstruction reliably increases MRF acquisition speed and accuracy.

INTRODUCTION

The recently proposed Magnetic Resonance Fingerprinting (MRF) technique allows fast and simultaneous acquisition of quantitative tissue parameters (1). In MRF, the temporal signal evolution follows a pattern (a “fingerprint”) assumed to be unique to a specific combination of quantitative parameters such as T1, T2 and PD. MRF can then quantify these parameters by comparing the acquired signal pattern to a dictionary of pre-simulated fingerprints based on the Bloch equations or another simulation method, such as extended phase graphs (2).

Corresponding Author: Mark Griswold, Bolwell Building Room B121, 11100 Euclid Avenue, Cleveland, OH 44106, USA, Phone: 216-844-8085, mark.griswold@case.edu.

This pattern matching operation is performed in (1) by selecting the fingerprint presenting the highest inner-product with the signal. This approach was shown to be robust to incoherent signal perturbations. This property can be used to acquire an image series at a very high sampling reduction factor (R), as long as the aliasing noise at each voxel is temporally incoherent with the signal of interest.

The parameter mapping strategy employed by MRF uses an analogous sparsity constraint to Compressed Sensing (CS) methods, which use a learned temporal signal dictionary or an *a priori* temporal evolution model to accelerate quantitative (3–5) and dynamic acquisitions (6,7). These CS reconstruction methods are iterative: the noise-like incoherent aliasing artifacts are gradually removed from the undersampled images until convergence to a sparse solution in good agreement with the acquired data (a process which we refer to as "image denoising"). In comparison the MRF method as presented in (1) is non-iterative: the quantitative maps are produced without denoising of the image series and there is no enforcement of data fidelity. As a result a large number of images must be acquired to correctly identify the noise-corrupted fingerprint. In essence MRF compensates a high R with additional temporal measurements. However once the temporal evolution of a pixel value is known, this knowledge can be exploited to reduce the aliasing noise generated by the pixel. Therefore if the undersampled images could be denoised, the number of images to acquire would be reduced, adding further speed and efficiency to the technique.

The objective of this work is to implement an efficient image-denoising method to decrease the number of repetition times needed for MRF acquisition. To this end an iterative multi-resolution CS reconstruction approach was chosen, in which the sources of mapping errors are reduced before gradually adding higher resolution information. The benefits of this approach are established for simultaneous mapping of T1, T2, PD and off-resonance frequency in both phantoms and *in vivo*.

METHODS

Reconstruction Algorithm

This work considers a series of L undersampled images **x** with N voxels obtained from a measured k-space signal **y**, each acquired with a pseudo-random schedule of Repetition Time (TR) and flip angle (FA). Each image $\mathbf{x}_t$ of **x** is obtained by $\mathbf{x}_t = \mathcal{F}^{-1}(\mathbf{y}_t)$, where $\mathbf{y}_t$ is the k-space measurement from the tth TR, and $\mathcal{F}^{-1}$ performs the inverse Fourier transform; or inverse non-uniform Fourier transform if the trajectory is non-Cartesian.

The MRF template matching process can then be viewed as a CS image denoising step for **x**:

$$\min \|\mathbf{x}-\mathbf{D}\mathbf{c}\|_2 \; with \; \|\mathbf{c}_\mathrm{p}\|_0=1, \quad 1 \leq \mathrm{p} \leq N, \quad [1]$$

where **D** (matrix of dimension L×M) is the dictionary of M fingerprints and **c** is a M×N sparse coefficient matrix. For pixel location p, the column $\mathbf{c}_\mathrm{p}$ of **c** reduces **D** to the best matching fingerprint and scales this fingerprint according to the estimated PD value. Equation [1] is analog to the sparse coding stage of the k-SVD algorithm (3,8) where only one atom of the dictionary is selected to approximate the temporal signal at a given pixel.

After solving for **c** in [1], the image series **x** can be updated based on **Dc** and **y** (3), and [1] can be solved in a new iteration.

This approach has been shown to successfully denoise images acquired at R=10 to 15 but starts to show limitations at higher reduction factors (3). In contrast, MRF image series are often acquired at R=48 or higher. Moreover, this work assumes a reduced MRF acquisition where L, the length of the image series, would lead to large errors with the original MRF implementation. If those errors are too numerous, the algorithm may not converge or could become stuck in a local minima. However, here we take advantage of the fact that CS and MRF acquisition trajectories can be more densely sampled in the center of k-space. Therefore it is possible to produce an image series **x** at a low resolution with an effectively smaller R for which [1] can be used for effective denoising.

In this work, a Gaussian weighting of k-space is used to produce this low resolution image series. For iteration i, let $\mathbf{G}^{(i)}$ be a matrix of the same dimensions as **y** whose elements follow a Gaussian distribution depending on their k-space location:

$$G_q^{(i)} = e^{-\frac{k_x(q)^2 + k_y(q)^2}{2\sigma_i^2}} \quad [2]$$

where $G_q^{(i)}$ is the qth element of $\mathbf{G}^{(i)}$. Then a low resolution image series $\mathbf{x}^{(i)}$ is easily produced by setting $\mathbf{y}^{(i)} = \mathbf{G}^{(i)} * \mathbf{y}$ and $\mathbf{x}_t^{(i)} = \mathcal{F}^{-1}(\mathbf{y}_t^{(i)})$, with * denoting element-wise multiplication. The effective resolution of $\mathbf{x}^{(i)}$ is then controlled by the standard deviation σ_i of the distribution. While equation [2] describes a distribution for a 2D acquisition, its extension to a 3D acquisition is trivial.

The following MRF denoising algorithm is proposed:

Initialization:

- Set $\mathbf{x}^{(0)} = \mathbf{0}$.
- Let k_{max} be the largest k-space distance to the origin sampled during the acquisition. Set σ_0 so that $\sigma_0 < k_{max}$.
- Set $\mathbf{y}^{(0)} = \mathbf{G}^{(0)} * \mathbf{y}$.

For iteration i:

1. Compute $\mathbf{x}_t^{(i)} = \mathcal{F}^{-1}(\mathbf{y}_t^{(i-1)})$ for all $t \in [1,L]$.
2. Find $\mathbf{c}_p^{(i)}$ so that $\mathbf{Dc}_p^{(i)} \approx \mathbf{x}_p(i)^{\dagger}$ and set $\tilde{\mathbf{x}}_p^{(i)} = \mathbf{Dc}_p^{(i)}$ for all $p \in [1,N]$.
3. Compute $\mathbf{y}_t^{(i)} = \mathcal{F}^{-1}(\tilde{\mathbf{x}}_t^{(i)})$ for all $t \in [1,L]$.
4. **a.** Set σ_i so that $\sigma_{i-1} < \sigma_i$.

   If $\sigma_i < k_{max}$, set $G_q^{(i)} = e^{-\frac{k_x(q)^2 + k_y(q)^2}{2\sigma_i^2}}$ for all element q of $\mathbf{G}^{(i)}$

   Else set $G_q^{(i)} = 1$ for all q

† this step is performed by selecting the fingerprint yielding the highest vector dot-product with $x_p^{(i)}$.

b. For all element q corresponding to a sampling location after Cartesian gridding, substitute $y_q^{(i)} = G_q^{(i)} y_q$.

5. Repeat steps 1 to 4 until a convergence criterion $\frac{\|\mathbf{x}^{(i)}-\mathbf{x}^{(i-1)}\|}{\|\mathbf{x}^{(i)}\|}<\varepsilon$ is reached.

Once convergence is reached, each column of the last computed **c** matrix is used to produce the quantitative parameter maps. A graphic representation of this algorithm is given in Figure 1, starting from the top. At initialization, Step 4b is bypassed, i.e., $\mathbf{y}^{(0)}$ is left zero-filled. As described above in Step 4, if $k_{max}<\sigma_i$ there is no Gaussian weighting and **y** is used at its maximum image resolution.

This algorithm is described here for a single receive coil acquisition. For a multi-coil acquisition, all $\mathbf{x}_t^{(i)}$ would be coil combined after Step 1, and estimated coil sensitivities would be applied on each $\tilde{\mathbf{x}}_t^{(i)}$ before Step 3. It should be noted that MRF performs a complex template matching which requires preserving the phase information of each temporal signal. Therefore coil combination should be performed by summing each channel image weighted by the complex conjugate of the coil sensitivities, instead of a simple sum-of-squares, for example.

Further image or transform sparsity could also be enforced in Step 2. For example, one could apply wavelet denoising (9) or total variation constraints either on $\mathbf{x}^{(i)}$ or $\tilde{\mathbf{x}}^{(i)}$ (10). Another approach offered by MRF is to apply wavelets or total variation-type constraints on the parameter maps themselves, which can be done much faster than on the entire image series. Indeed, parameter maps can be obtained from $\mathbf{x}^{(i)}$ at any iteration. The denoising scheme of choice can then be applied on these parameter maps (9,10). Then for each pixel location p, $\tilde{\mathbf{x}}_p^{(i)}$ can be obtained by assigning the temporal signal evolution equal to the database fingerprints with the closest parameters to the denoised parametric maps.

For purposes of clarity, the algorithm described above will be referred to as Iterative Multi-Scale MRF (IMS-MRF). The MRF method as proposed in (1) will be referred to as "original MRF". It should be noted that the original MRF method corresponds to a single iteration of IMS-MRF without any Gaussian weighting.

MRF parameters

The MRF acquisition parameters used for this work are given in Figure 2. Figure 2a–b shows the variations in TR length and FA for 3000 undersampled image acquisitions. The phase of the excitation pulse alternates by 180° between two consecutive acquisitions. A Variable Density Spiral (VDS) trajectory was used to sample k-space after each excitation pulse (Figure 2c). The zero and first order moments of the trajectory (solid and dashed lines) were zero, and the slice excitation gradients were balanced. The k-space samples used for image reconstruction are shown in full lines. With respect to Nyquist sampling, the trajectory had R =24 within a radius of 25% of k_{max} from the center of k-space, and R=48 outside of this radius. The VDS trajectory was rotated by $2\pi/48$ radians after each TR. The Field of View (FOV) was 300mm and the matrix size 256×256.

The dictionary **D** of fingerprints was calculated based on the pulse sequence schedule described above using Bloch equations as in the original MRF work. The simulated T1 and T2 values were chosen to span typical ranges found in brain tissues. Simulated T1 values ranged from 100 to 1000 ms in increments of 20 ms, from 1000 to 2000 ms in increments of 50 ms, and from 2000 to 5000 ms in increments of 300 ms. Simulated T2 values went from 20 to 110 ms in increments of 10 ms, from 110 to 300 ms in increments of 20 ms, and from 300 to 2000 ms in increments of 200 ms. B_0 field inhomogeneity (ΔB_0) was also included in the simulations, with ranges from −60 to 60 Hz by increments of 1 Hz, and −300 to −150 Hz and 150 to 300 Hz by increments of 20 Hz. Combination of T1 and T2 values where T1<T2 were excluded, leading to a total of 186046 fingerprints.

All numerical computations and simulations for this work were performed in Matlab R2012b programming environment (The Mathworks, Natick, MA) on a personal computer with 2.0GHz Intel Xeon CPU and 32 GB RAM.

Numerical Phantom Study

The proposed IMS-MRF was first tested on a numerical brain phantom, using the numerical T1, T2 and PD maps obtained from the MNI brain atlas (11,12). A ΔB_0 field was arbitrarily simulated as a linear variation from −60 to +60 Hz, from left to right. A series of 3000 images was produced by simulating the signal evolution on a pixel-wise basis based on the parameter values and the pulse sequence described above. Complex normally distributed noise was added to the image series to simulate a peak SNR of 100, calculated within a ROI mask of the numerical brain. The mean±standard deviation SNR within the same ROI for the fully-sampled image series was 17.5±8.9. The non-uniform Fast Fourier Transform (nuFFT) was applied on each image to the corresponding VDS trajectory to simulate the matrix of undersampled k-space measurements. In this work, all nuFFT and inverse nuFFT operations were done using the image reconstruction toolbox provided by Jeffrey Fessler (13).

Quantitative maps of T1, T2, ΔB_0 and PD were computed with IMS-MRF from series of the first 300, 500, 1000, 2000 and 3000 simulated spiral measurements. The standard deviation for the Gaussian weighting was chosen empirically as $\sigma_0=0.125k_{max}$, $\sigma_1=0.25k_{max}$ and $\sigma_2=0.75k_{max}$ respectively at initialization, first and second iteration. No Gaussian weighting was applied on subsequent iterations (i.e. $\sigma_i>k_{max}$ in step 4 described above). The convergence criterion was $\varepsilon=0.5\%$, calculated within the numerical mask. Quantitative maps were also computed with original MRF for comparison. To illustrate the ability of the multi-resolution approach to avoid local minima, quantitative maps were also computed from a series of 300 spirals using the proposed algorithm without any Gaussian weighting (referred to as “purely iterative MRF”). The benefit of further constraints was also evaluated by applying wavelet (WV) denoising on quantitative maps with automated thresholding selection (9) using the same image series. The performance evaluation function for all parameters was chosen as the Root Mean Square Error Normalized by the dynamic range of the image (NRMSE).

To reduce computational time, pixel-wise MRF template matching was only performed within the mask of the numerical brain.

Agar Phantom Study

While the numerical phantom experiment allows quantification of the denoising performance of IMS-MRF on the aliased images of a complex object such as a brain, the quantification of the accuracy of IMS-MRF in a more realistic acquisition setting is also desirable. To this end an undersampled image series was acquired from ten $GdCl_3$ and Agarose phantoms with the above MRF sequence and 3000 undersampled image acquisitions at 3T on a Siemens Skyra (Erlangen, Germany), using 8 channels of a head coil array.

The phantom T1 values were first measured with a standard single Spin-Echo (SE) inversion recovery experiment with TR=6s, echo time (TE) of 12ms and seven different inversion times (TI) of 50, 100, 200, 500, 1000, 2000 and 3500ms, for a total acquisition time of 42 min. The T2 values were measured with single-echo SE with TR=6s using eight different TE of 20, 40, 60, 100, 150, 200, 400 and 800ms, for a total time of 48 min. The T1 and T2 values of the phantoms ranged from 200 to 1500ms and 30 to 110ms, respectively.

The acquired MRF images were summed together to produce a fully sampled composite image, from which an estimate of the coil sensitivities was computed using the adaptive combination method (14). A ROI mask of the composite image was produced using Otsu's automatic segmentation method (15).

T1 and T2 maps were computed with the IMS-MRF and original MRF using the first 300, 500, 1000, 2000 and 3000 undersampled images. All template matching computations were performed within the ROI mask. The mean value and standard deviation for each parameter was computed within an ROI for each phantom. Concordance correlation coefficients (16) between the measured parameter values and the corresponding SE measurements were calculated for original and IMS-MRF for each image series length.

In Vivo Study

Finally the proposed algorithm was tested to perform brain tissue parameter mapping on *in vivo* data. An undersampled brain image series was acquired from a healthy volunteer with the above MRF sequence and 3000 undersampled image acquisitions on the same 3T scanner as the phantom experiment. In this Institutional Review Board approved and HIPAA-compliant study, informed consent was obtained from the volunteer prior to the experiment. Parameters maps for T1, T2, ΔB_0 and PD were produced with original MRF and IMS-MRF using the first 500, 1000, and 3000 undersampled image acquisitions. As an approximate measure of quantification error, maps produced from 3000 images were chosen as a reference to compute an NRMSE.

RESULTS

Numerical Phantom Study

Figure 3a compares the ground truth T1 and T2 maps (left) with the maps obtained using IMS-MRF (middle), and using purely iterative MRF (right) from a series of 300 simulated images. Without a multi-scale approach, the recovered maps are entirely corrupted with

errors. In contrast, the IMS-MRF T1 and T2 maps are in good agreement with the ground truth, though T2 maps have more substantial errors. The algorithm's convergence behavior of IMS-MRF and purely iterative MRF are displayed in Figure 3b–c. Figure 3b plots the T2 NRMSE against the number of iterations. Purely iterative MRF shows a decrease of errors after iteration 1, and the NRMSE appears the same between iteration 1 and 2, but the maps actually changed with each iteration and eventually diverged out of their local minima. In contrast, IMS-MRF led to consistent improvement until convergence within 7 iterations. These convergence behaviors are illustrated in Fig 3c with the corresponding T2 maps after initialization, iteration #3, iteration #6 and the last computation iteration.

Figure 4 plots the relative error of original MRF, IMS-MRF and IMS-MRF with wavelet denoising for each parameter against the acquisition length, i.e. the sum of all TR values in the series. As expected for original MRF, all NRMSE values decrease with longer acquisition, with lowest NRMSE reached with L=3000. It should be noted that the NRMSE curves for IMS-MRF and MRF did not converge to the same value for L=3000, with a slightly lower NRMSE for IMS-MRF. Supporting Figure S1 (available online) shows the corresponding error maps for T1 and T2 at L=3000. For both original MRF and IMS-MRF, the residual differences are constrained to the boundaries between tissues, where partial volume effects can occur. These residual errors are consistently reduced for IMS-MRF, and are on the order of dictionary quantization error (lower than 6% for T1, and lower than 10% for T2).

For all parameters, the NRMSE of IMS-MRF was lower with L=500 (5.1 s total acquisition length) than for the original MRF with L=3000 (30.9s total acquisition length). The NRMSE of IMS-MRF slightly improved with L=1000, but remained almost unchanged with a higher L. At L=300 (3.0 s), the additional use of wavelet denoising performed worse than IMS-MRF alone, but a slight improvement in T2 and ΔB_0 was observed with L=500.

Figure 5 shows a comparison of maps obtained with original MRF (top row), IMS-MRF (middle row), and IMS-MRF with additional wavelet denoising (bottom row) for L=500 (10.2 s total acquisition time). While the original MRF was able to recover a T1 maps with little apparent errors, other parameter maps are severely contaminated with artifact errors. These artifacts are almost entirely removed with both iterative approaches. Additional use of wavelet denoising provided an improvement of small residual errors in T2 and ΔB_0 maps in the right-anterior part of the brain (see arrows).

The computational time to convergence for each L are compiled in Table 1. The method converged in 7 iterations for L ≤1000, and 5 iterations for higher L.

Agar Phantom Study

T2 maps of the agar phantoms obtained with Original MRF (a) and IMS-MRF (b) for various values of L can be seen in Figure 6, along with corresponding error maps. IMS-MRF appears to be more robust to aliasing noise than the original MRF particularly for phantoms with low T2 values, even with a small L. Figure 7a plots T1 (left) and T2 (right) values measured with original MRF (red triangles) and IMS-MRF (blue circles) using L=1000. The value measured with SE is used as the abscissa value, and the solid line represents the

identity. While T1 and T2 values were in good agreement with SE values for all methods, all T2 values measured with IMS-MRF display identical or slightly reduced deviation from SE values. This improvement is clearer in Figure 7b, when L=300. The error bars indicate the parameter error standard deviation in each ROI for a given GdCl3 and Agarose phantom with respect to the ground truth parameter value. As can be seen in figure 6a for the original MRF method at L=300, some phantoms are much more subject to mapping errors than others, leading to higher error bars in figure 7. This variability in parameter mapping accuracy from phantom to phantom is reduced with IMS-MRF. Figure 7c plots the concordance correlation coefficient with SE values for both methods against the length of the acquisition. For L>1000, the concordance correlation coefficient is over 0.99 for both methods. For L<1000, the T2 concordance coefficient starts to markedly decrease for original MRF, while it stays over 0.99 for IMS-MRF. Please note that the matrix size in this work is 256×256, while the original MRF work presented in (1) was performed at a matrix size of 128×128.

In Vivo Study

Figure 8 shows three sample images from the in vivo image series with and without denoising (top and bottom row, respectively) with L=500 for the proposed denoising algorithm after convergence (7 iterations). The acquisition time for each displayed image did not exceed 11ms. In the top row, the images used by the original MRF are entirely contaminated by aliasing noise. After denoising, anatomical features are clearly visible, though the noise level remains high. A video comparing the entire image series is available online as supplementary material (see Supporting Video).

A comparison of all four parameter maps obtained with the original MRF and IMS-MRF methods for acquisition L= 500, 1000 and 3000 is displayed in Figure 9. The NRMSE of the L=500 and L=1000 maps compared to their L=3000 counterparts are shown as inset. For original MRF with L=3000, a small number of outlier pixels can be seen close to the ventricles for all parameter maps. These artifacts become more apparent when L=1000 and clearly mask anatomical information when L=500. IMS-MRF with L=500 produced T1 maps with 0.5% lower NRMSE than the original MRF with L=1000. For other tissue parameters, the NRMSE with IMS-MRF and L=500 was never more than 1.2% higher than their original MRF counterpart with L=1000.

In comparison, no clear artifact is visible on IMS-MRF maps with either L=1000 or L=3000. When only L=500 are used, most of the severe artifacts seen in original MRF maps are not present in IMS-MRF maps. Some remaining artifacts can be seen in the anterior region of the maps, particularly for ΔB_0 maps. However, T1 and T2 maps maintained a low NRMSE compared with maps obtained using a 6 times longer acquisition.

DISCUSSION

Many approaches exist to the denoising problem posed by the undersampled MRF acquisition. With a straightforward iterative method at full resolution, the large amount of aliasing can lead the algorithm to reach an unstable local minimum. While such an approach could converge for a higher level of sampling in k-space and/or through time, the proposed

multiscale approach offers a good convergence behavior with as few as L=300 at an acceleration factor of 48, at the price of a simple element-wise multiplication in k-space. While the proposed multi-scale approach avoided convergence to undesirable local minima in our experiments, other MRF sequence designs may require additional regularization to reach acceptable solutions. The proposed framework is quite flexible and can accommodate other constraints in addition to MRF sparse encoding. In this work, additional WV denoising was tested on simulated data. The benefits in reconstruction quality appeared small compared to the increase in computational time, and for a very small L, these additional constraints actually worsened the parameter map quality. However, other sparsity constraints may prove more useful. Due to the nature of MRF, all parameters maps are strongly linked, i.e. quality improvement achieved for one parameter map can induce quality improvement for another parameter map. Therefore, additional constraints on only one parameter map could be considered such as only enforcing smoothness of the ΔB_0 maps. One can note that the strong Gaussian weighting of the proposed algorithm enforces such smooth variations on the first iterations, albeit for all maps.

The lengthy computational time of the proposed method is mostly due to the high number of NUFFT operations introduced by the algorithm. In an attempt to speed up the reconstruction process the tested implementation incremented σ_i in large steps so as to reach convergence faster. In particular we empirically chose k_{max} as the highest value for σ_i, leading to a rather large jump in effective resolution when Gaussian filtering is no longer applied. Other approaches could include implementing smaller σ_i steps up to a higher threshold than k_{max}, at the price of more iterations and lengthier computations. The best update schedule will likely depend on the particular application. However, performing these operations with a Graphics Processing Unit or other highly parallel implementation in a compiled language, such as C as compared to Matlab, could allow for clinically acceptable reconstruction times (17).

Unlike the original MRF method, the proposed algorithm maintains excellent T1 and T2 accuracy for acquisition times as short as 3s with L=300. This reduction in acquisition time would have obvious benefits for patient comfort, in particular if the examination is performed with breath-holding for abdominal quantitative imaging. The time gains could also be reinvested to increase the number of slices acquired within the same acquisition time. Additionally, shorter dictionary fingerprints would also ease the computational requirements for future optimization of the pattern recognition steps in MRF. Our experience shows that L=300 is close to the minimum for IMS-MRF data of this resolution and dictionary resolution. Below this level, the performance of this method decays away rapidly.

In MRF acquisitions, the strength of the aliasing noise in the image series is inherently dependent on the type of tissues and their distribution in the FOV. For example, the mapping accuracy at the center of the FOV can be expected to be worse than at its periphery in certain cases, as can be seen in figure 6 and 7. By reducing the aliasing noise, IMS-MRF also reduces this type of error variability. It should be noted that this method provided an increase in the quality of the maps even near the edges of tissues, even in cases where partial volume effects could be present. Further improvement in future studies could potentially be obtained

using more sophisticated partial volume separation methods previously described for MRF (1,18).

For in vivo brain imaging, IMS-MRF allows artifact free mapping of T1, T2, PD and ΔB_0 at 256×256 matrix resolution with a 10.2s long acquisition. The original MRF method typically requires L>3000 (>30.6 s) to produce such artifact free maps without parallel imaging or other speed-up methods. With L=500, IMS-MRF can produce T1 and T2 maps in good agreement with maps obtained from twice the acquisition length.

CONCLUSIONS

An image denoising framework was implemented which improves MRF acquisition speed by iteratively enforcing dictionary sparse encoding and data consistency. Even for a highly reduced number of samples, the proposed algorithm can converge to a reasonable solution by using the more densely sampled center of k-space in the first iterations before gradually including higher spatial harmonics in the data consistency step. A potential 3 to 6-fold reduction in acquisition time was demonstrated in comparison to the original MRF method. Further acceleration and improvement of parameter mapping accuracy could be achieved by using additional constraints. The reduction in the required number of undersampled acquisitions could also render the fingerprint dictionary optimization problem of MRF less computationally intensive.

Supplementary Material

Refer to Web version on PubMed Central for supplementary material.

Acknowledgments

This work was supported in part by NIH grant 1R01EB016728 and Siemens Healthcare.

The authors would also like to thank Dr. Katherine Wright for her feedback and editorial review.

References

1. Ma D, Gulani V, Seiberlich N, Liu K, Sunshine JL, Duerk JL, Griswold Ma. Magnetic resonance fingerprinting. Nature. 2013; 495:187–92. [PubMed: 23486058]
2. Hennig J, Weigel M, Scheffler K. Calculation of flip angles for echo trains with predefined amplitudes with the extended phase graph (EPG)-algorithm: principles and applications to hyperecho and TRAPS sequences. Magn Reson Med. 2004; 51:68–80. [PubMed: 14705047]
3. Doneva M, Börnert P, Eggers H, Stehning C, Sénégas J, Mertins A. Compressed sensing reconstruction for magnetic resonance parameter mapping. Magn Reson Med. 2010; 64:1114–1120. [PubMed: 20564599]
4. Huang C, Graff CG, Clarkson EW, Bilgin A, Altbach MI. T2 mapping from highly undersampled data by reconstruction of principal component coefficient maps using compressed sensing. Magn Reson Med. 2012; 67:1355–66. [PubMed: 22190358]
5. Block KT, Uecker M, Frahm J. Model-based iterative reconstruction for radial fast spin-echo MRI. IEEE Trans Med Imaging. 2009; 28:1759–69. [PubMed: 19502124]
6. Liang Z-P. Spatiotemporal Imaging with Partially Separable Functions. 2007; 2:988–991.
7. Christodoulou AG, Brinegar C, Haldar JP, Zhang H, Wu Y-JL, Foley LM, Hitchens T, Ye Q, Ho C, Liang Z-P. High-resolution cardiac MRI using partially separable functions and weighted spatial

smoothness regularization. Proceedings ot the Annual International Conference of the IEEE Engineering in Medicine and Biology Society. 2010; 2010:871–4.

8. Aharon M, Elad M, Bruckstein A. K -SVD: An Algorithm for Designing Overcomplete Dictionaries for Sparse Representation. IEEE Trans signal Process. 2006; 54:4311–4322.
9. Donoho DL, Johnstone IM. Ideal Spatial Adaptation by Wavelet Shrinkage. Biometrika. 1994; 81:425–455.
10. Lustig M, Donoho DL, Santos JM, Pauly JM. Compressed Sensing MRI. IEEE Signal Process Mag. 2008; 25:72–82.
11. Holmes CJ, Hoge R, Collins L, Woods R, Toga AW, Evans AC. Enhancement of MR Images Using Registration for Signal Averaging. J Comput Assist Tomogr. 1998; 22:324–333. [PubMed: 9530404]
12. Aubert-Broche B, Evans AC, Collins L. A new improved version of the realistic digital brain phantom. Neuroimage. 2006; 32:138–45. [PubMed: 16750398]
13. Pipe, JG. Matlab nuFFT Toolbox. http://web.eecs.umich.edu/~fessler/code/
14. Walsh DO, Gmitroa F, Marcellin MW. Adaptive reconstruction of phased array MR imagery. Magn Reson Med. 2000; 43:682–90. [PubMed: 10800033]
15. Otsu N. A tlreshold selection method from gray-level histograms. Automatica. 1975; 11:285–296.
16. Lin L. A concordance correlation coefficient to evaluate reproducibility. Biometrics. 1989; 45:355–368.
17. Saybasili H, Herzka Da, Seiberlich N, Griswold Ma. Real-time imaging with radial GRAPPA: Implementation on a heterogeneous architecture for low-latency reconstructions. Magn Reson Imaging. 2014; 32:747–758. [PubMed: 24690453]
18. Deshmane, AV.; Ma, D.; Jiang, Y.; Fisher, E.; Seiberlich, N.; Gulani, V.; Griswold, Ma. Validation of Tissue Characterization in Mixed Voxels Using MR Fingerprinting. Proceedings of the 22nd Annual Meeting of ISRMRM; 2014; p. 94

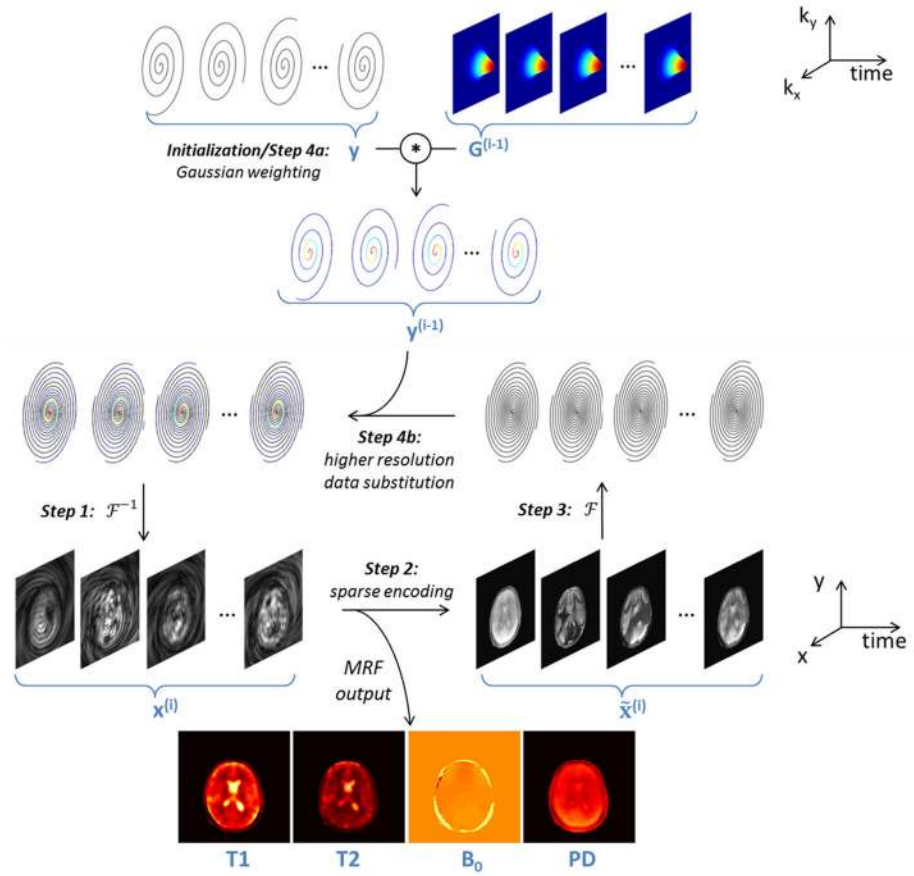

Figure 1.

Illustration of the iterative multi-scale algorithm: Starting from the top, the zero-filled measured k-space is Gaussian weighted at initialization. **Step 1:** $\mathbf{y}^{(i-1)}$ is inverse-Fourier transformed, yielding $\mathbf{x}^{(i)}$. **Step 2:** MRF template matching is performed to denoise image series. If $\mathbf{x}^{(i)}$ had converged, stop here and output corresponding maps. **Step 3:** The denoised image series is Fourier transformed, yielding $\mathbf{y}^{(i)}$. **Step 4:** A new iteration starts, with a weaker Gaussian weighting of the original data and its direct substitution for the acquired elements of $y^{(i)}$ at their sampled locations after Cartesian gridding.

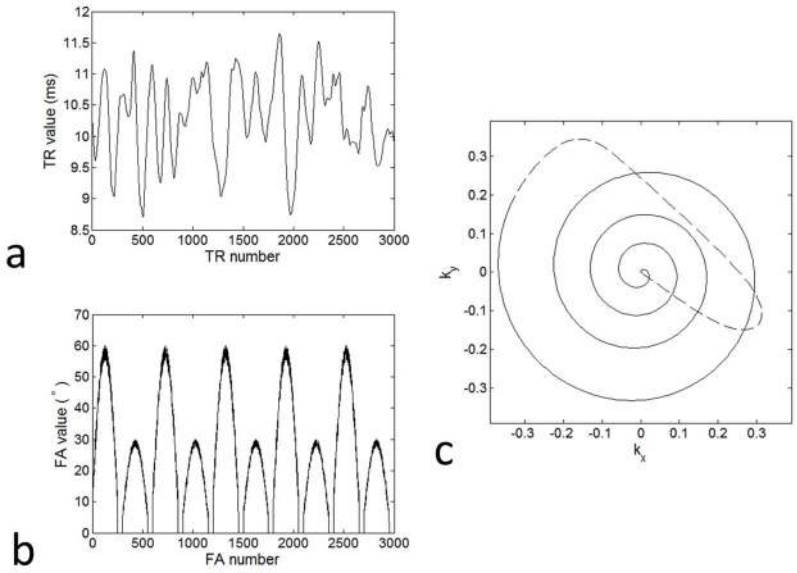

Figure 2.

MRF sequence parameters. **a.** Sequence of pseudo random TR values. **b.** Sequence of FA values for each excitation pulse. **c.** example VDS trajectory. Only measurements sampled along the full line were used for image reconstruction.

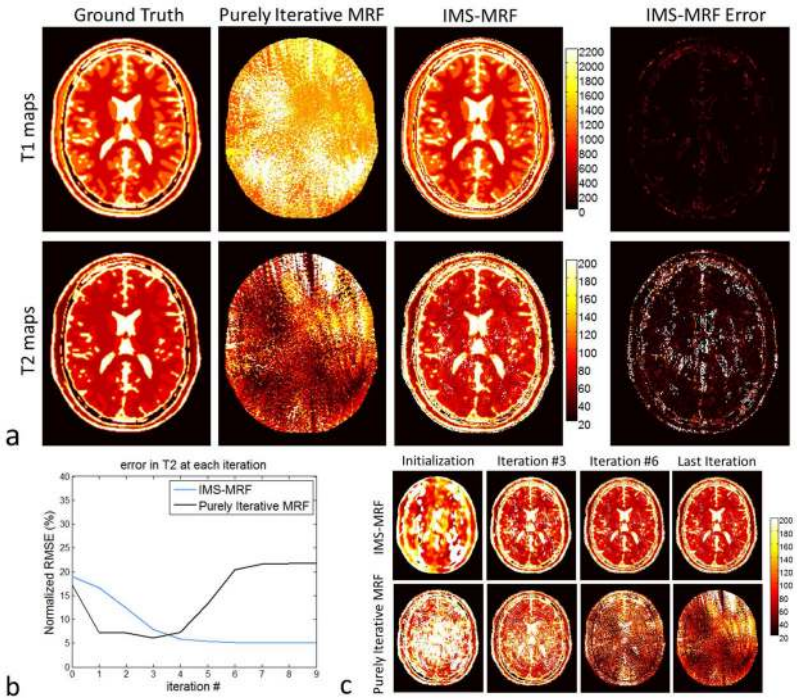

Figure 3.

a. Comparison of T1 and T2 maps (upper and lower row, respectively) obtained after convergence of IMS-MRF (3rd from left) purely iterative MRF (2nd from left) to their respective ground truth (left). Error maps shown on the right. **b.** T2 normalized RMSE evolution with each iteration of IMS-MRF (light blue) and purely iterative MRF (black). **c.** From left to right, T2 maps obtained after initialization, iteration 3, iteration 6 and the last iteration of IMS-MRF (top row) and purely iterative MRF.

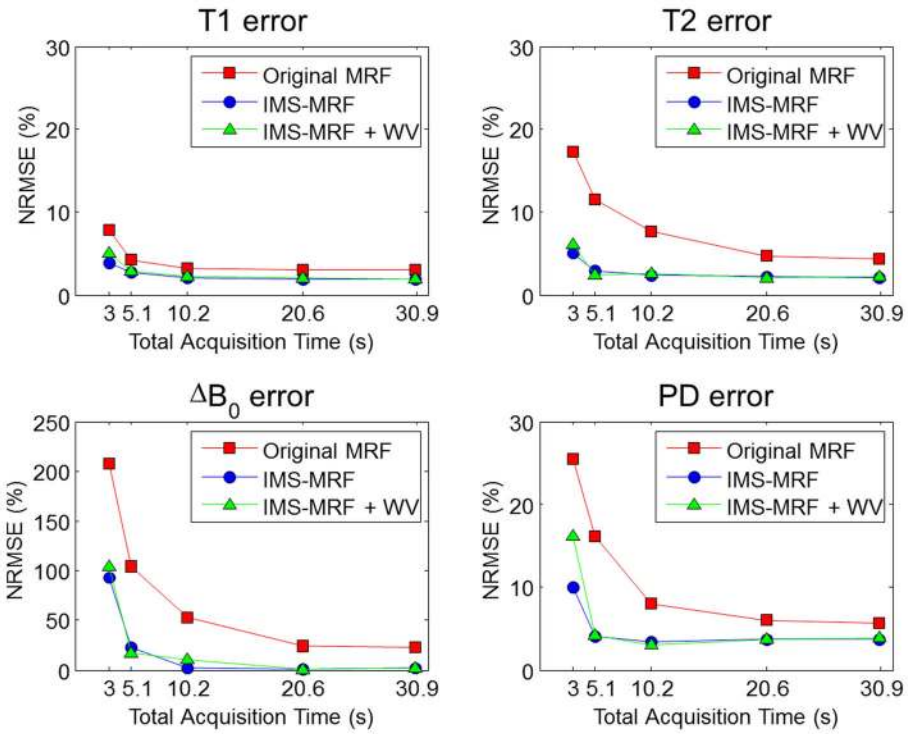

Figure 4.

Normalized RMSE evolution with total acquisition time for each parameters. Original MRF values are displayed in red squares, IMS-MRF in blue circles and IMS-MRF with WV denoising in green triangles.

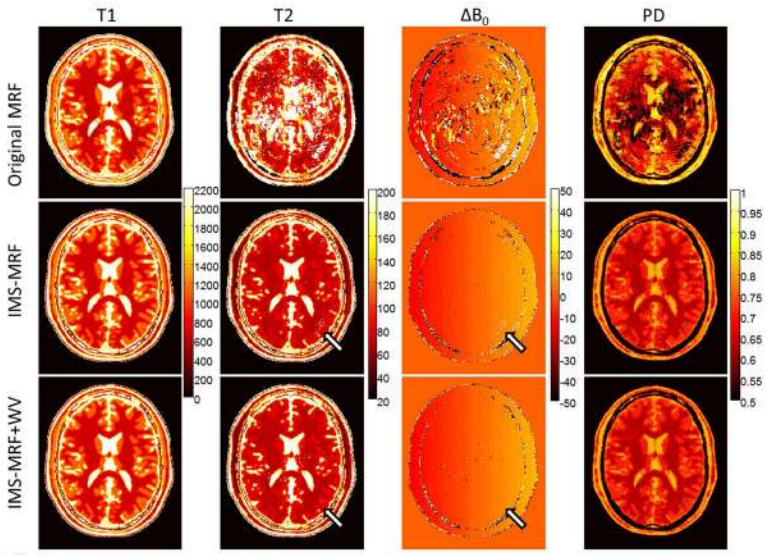

Figure 5.

Maps of T1, T2, ΔB_0 and PD obtained with L=500 (5.1 s total acquisition) for Original MRF (top row), IMS-MRF (middle row) and IMS-MRF with WV denoising (bottom row). Reductions of residual errors in T2 and ΔB_0 maps for IMS-MRF with WV are indicated by arrows.

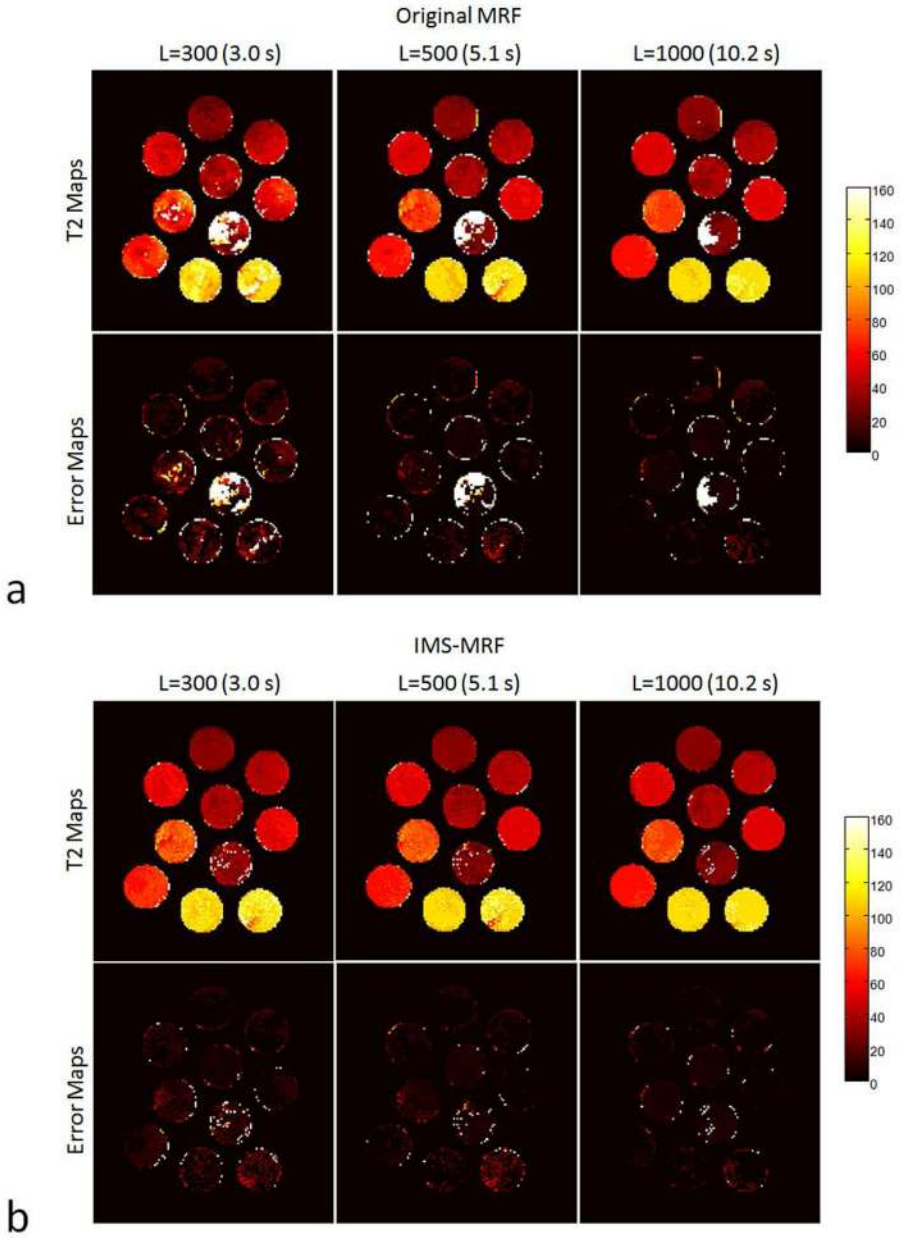

Figure 6.

T2 maps (top row) and corresponding error maps (bottom row) obtained with original MRF (a) and IMS-MRF (b) using the first 300 TRs (left), 500 TRs (middle) and 1000 TRs (right).

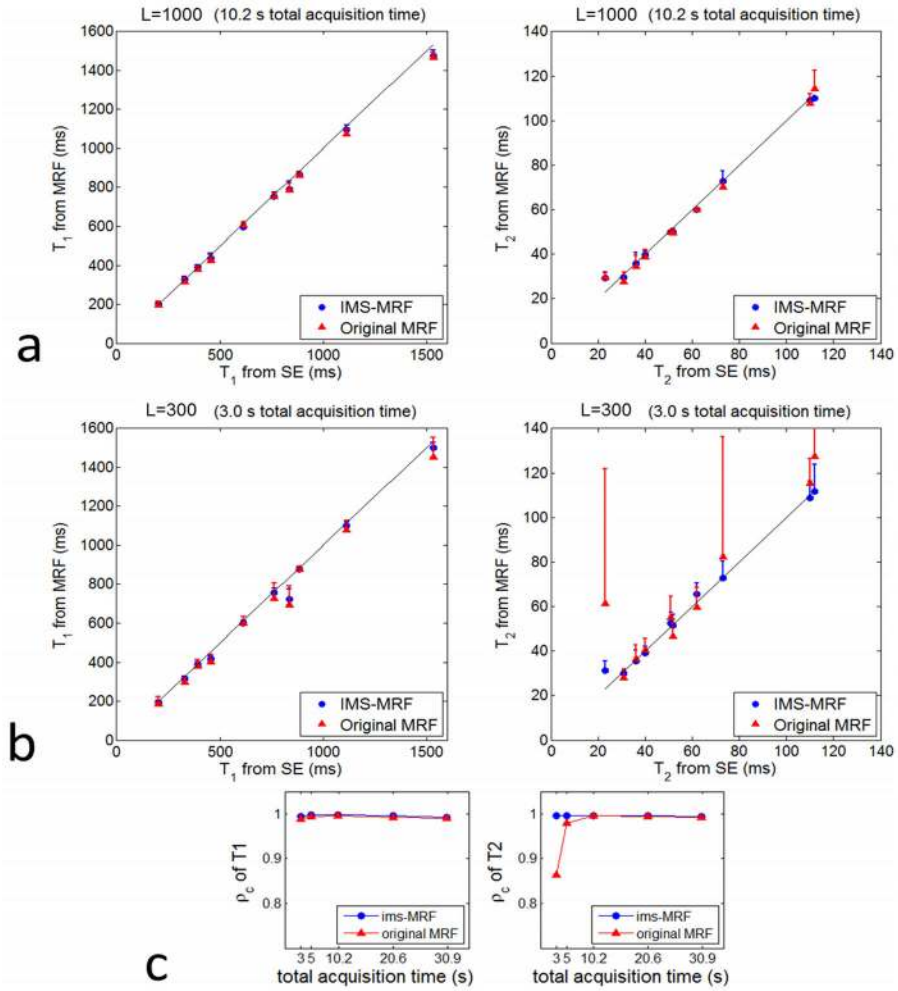

Figure 7.

Measured T1 (left) and T2 (right) comparison between SE and MRF measurements for **a.** 1000 TRs (10.2 s total acquisition time) **b.** 300 TRs (3.0 s total acquisition time) **c.** Evolution of the concordance coefficient with length of acquisition.

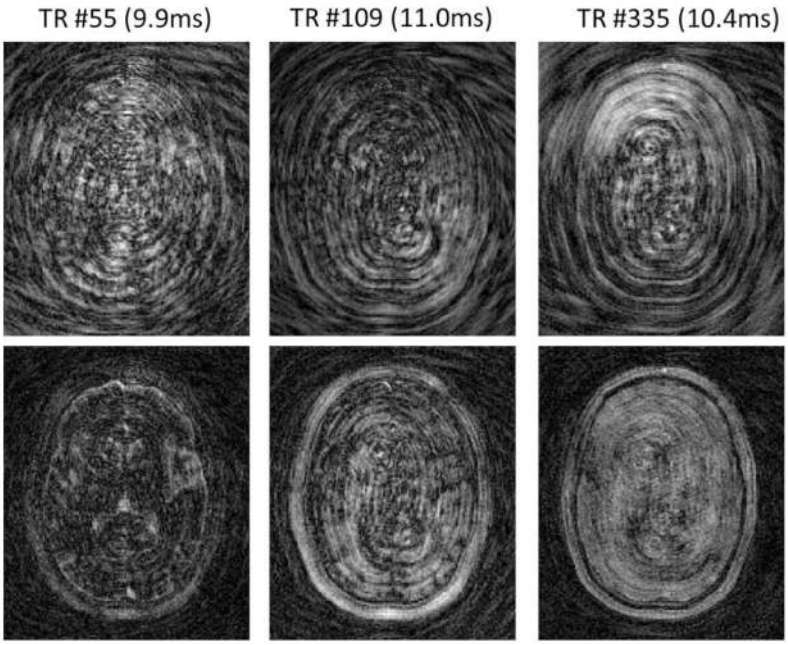

Figure 8.

In vivo images from the 55th TR (left column), 335^{h} TR (middle column) and 717th TR (right column) used to perform template matching with the original MRF method (top row) and IMS-MRF (bottom row) with 500 TRs. The duration of each TR is shown in parenthesis.

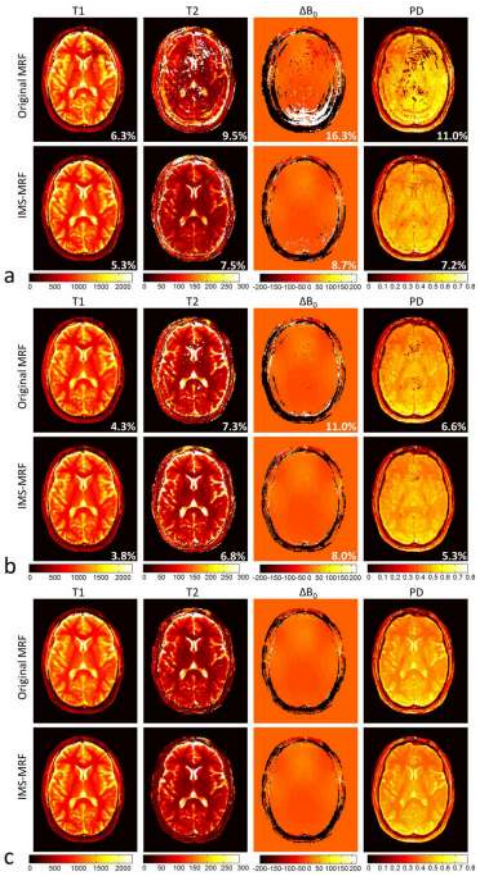

Figure 9.

In vivo parameter maps from the original MRF (top row) and IMS-MRF methods (bottom row) for L =500 (a), 1000 (b) and 3000(c). The NRMSE of the L=500 and L=1000 maps compared to their L=3000 counterparts are shown as inset.

Table 1

Computational time for each mapping method (single-threaded Matlab, one 2D slice).

	L=300	L=500	L=1000	L=2000	L=3000
Original MRF	3′08″	3′46″	5′14″	8′16″	6′51″
IMS-MRF	27′57″	40′46″	1h03′04″	1h51′16″	2h54′19″
IMS-MRF + WV	38′9″	52′26″	1h31′20″	2h49′44″	3h50′8″